ENGINEERING

Multivariate patterning of human pluripotent cells under perfusion reveals critical roles of induced paracrine factors in kidney organoid development

Nick R. Glass[1], Minoru Takasako[2,3]*, Pei Xuan Er[2,3], Drew M. Titmarsh[1†], Alejandro Hidalgo[1], Ernst J. Wolvetang[1,4], Melissa H. Little[2,3,5‡], Justin J. Cooper-White[1,4,6,7‡§]

Creating complex multicellular kidney organoids from pluripotent stem cells show great promise. Further improvements in differentiation outcomes, patterning, and maturation of specific cell types are, however, intrinsically limited by standard tissue culture approaches. We describe a novel full factorial microbioreactor array–based methodology to achieve rapid interrogation and optimization of this complex multicellular differentiation process in a facile manner. We successfully recapitulate early kidney tissue patterning events, exploring more than 1000 unique conditions in an unbiased and quantitative manner, and define new media combinations that achieve near-pure renal cell type specification. Single-cell resolution identification of distinct renal cell types within multilayered kidney organoids, coupled with multivariate analysis, defined the definitive roles of Wnt, fibroblast growth factor, and bone morphogenetic protein signaling in their specification, exposed retinoic acid as a minimal effector of nephron patterning, and highlighted critical contributions of induced paracrine factors on cell specification and patterning.

INTRODUCTION

The mammalian kidney is derived from the intermediate mesoderm (IM), arising via the inductive interactions between several key progenitor IM subpopulations. The anterior IM-derived epithelial nephric duct gives rise to a ureteric epithelium (UE), which forms the ureter and collecting ducts of the kidney. Conversely, the nephrons form via the epithelial transformation of the metanephric mesenchyme (MM), a derivative of the posterior IM. This understanding of normal mammalian kidney development has produced protocols for the directed differentiation of human pluripotent stem cells (hPSCs) toward kidney cell types, as reported by us (*1*–*3*) and others (*4*–*7*). Most protocols initially pattern to primitive streak to form trunk mesoderm; however, the formation of collecting duct-like epithelium (*4*) and MM and subsequent nephron patterning and segmentation have been reported (*5*–*8*).

After initial patterning to posterior primitive streak, the simultaneous induction of both a UE and a MM results in the generation of early nephrons (*1*). A slightly more posterior IM can be patterned after 7 days of monolayer culture, which, after dissociation, reaggregation and culture under three-dimensional (3D) culture conditions, self-assembles into kidney organoids with segmenting nephrons, collecting duct epithelium, endothelial progenitors, and surrounding renal interstitium (*3*). During the first 7 days of monolayer culture, only two inductive cues are used, an initial primitive streak patterning using a canonical Wnt pathway activator molecule, CHIR99201, followed by the addition of fibroblast growth factor 9 (FGF9). It is unclear whether the concentration of these molecules is optimal or whether they induce cell fate specification directly, synergistically, or through paracrine mechanisms. Nor is it clear whether particular combinations of factors can bias differentiation into specific subtypes of the developing kidney and how this is temporally modulated. Unfortunately, static cell culture practices provide only limited access to probe these parameter spaces. Expensive infrastructure, such as automated liquid handling–based cell culture systems, can begin to address these shortcomings, but because of their intrinsic static nature, they remain limited in terms of facilely probing and deciphering combinatorial, temporal, and paracrine influences on cell fate (*8*).

Microfabricated devices can overcome these limitations of static culture and have been successfully applied to classical biological challenges including single-cell polymerase chain reaction (*9*, *10*), on-chip in situ sensing (*11*–*13*), cell coculture (*14*), and subcellular isolation (*15*). This has permitted unprecedented investigation of complex biological phenomena, including mimicking perfusion rates during tissue patterning while using smaller volumes of reagents and substantially reducing experimental cost. Microdevices can be designed to multiplex experiments, allowing for a large number of experiments to be simultaneously performed on a single device (*16*). These "microbioreactor arrays" (MBAs) offer the opportunity to increase the parameter space and decrease the time frame of the protocol optimization and development (*17*, *18*). When combined with advanced quantitative image processing, the full potential of MBAs to facilitate systematic and unbiased assessment of multiple parameters aimed at optimization of differentiation conditions is unlocked. Various microfluidic arrays for cell culture have been developed; however, most of these devices offer either a low number of culture conditions or high levels of operational complexity (*19*–*22*).

[1]Australian Institute for Bioengineering and Nanotechnology, The University of Queensland, St. Lucia, QLD 4072, Australia. [2]Institute for Molecular Bioscience, The University of Queensland, St. Lucia 4072, Australia. [3]Murdoch Children's Research Institute, Flemington Rd., Parkville, VIC 3052, Australia. [4]UQ Centre in Stem Cell and Regenerative Engineering, The University of Queensland, St. Lucia, QLD 4072, Australia. [5]Department of Pediatrics, University of Melbourne, Parkville, VIC 3052, Australia. [6]Biomedical Manufacturing, Manufacturing Flagship, CSIRO, Clayton, VIC 3169, Australia. [7]School of Chemical Engineering, The University of Queensland, St. Lucia, QLD 4072, Australia.
*Present address: RIKEN Center for Biosystems Dynamics Research, Kobe, Japan.
†Present address: Scaled Biolabs Inc., San Francisco, CA, USA.
‡These authors contributed equally to this work as senior authors.
§Corresponding author. Email: j.cooperwhite@uq.edu.au

A valveless, full factorial, perfused MBA that uses resistive flow splitting through a nested and scalable fluid resistance network to allow for parallel analysis of 27 distinct media compositions, produced from the factorial combination of three different factors at three different combinations in the same base media, was recently reported (*23*–*25*). In this perfused device platform, an arrangement of 10 serially connected wells along each of the 27 columns facilitates the investigation of paracrine signals from upstream wells (fig. S1). Because of media being perfused from the top well to subsequent wells in of the 27 columns, each well is seeing not only the discrete basal media composition specific to that column but also the secreted factors from preceding wells, affording 270 unique, perfused culture conditions in the device. This system has previously been applied to pluripotent stem cell cultures, highlighting the key components in the maintenance of pluripotency (*25*), optimization of the maintenance of mesenchymal stem cells (*26*) and their differentiation toward an osteogenic fate (*27*), the optimization of long-term culture of self-renewing pancreatic progenitors derived from hPSCs (*28*), and differentiation of hPSCs to primitive streak lineages (*23*).

Here, we report the application of our MBA-based methodology to achieve unbiased, factorial assessment of the differentiation of hPSC-derived IM progenitors to multiple renal cell lineages and their subsequent patterning into multicellular kidney organoids. Custom postprocessing algorithms were developed to quantitatively analyze image cytometry outputs to phenotype, at single-cell resolution, the cellular composition and self-organized patterning induced in all 270 unique conditions for each MBA configuration and to deconvolute complex multicellular responses to the differentiation cues (*29*, *30*). This MBA platform approach both validated previously published protocols for the generation of renal lineages and identifies previously unappreciated critical impacts of paracrine signaling and roles for bone morphogenetic protein 7 (BMP7) and prolonged Wnt activation in renal cell fate decisions, lineage bias, and organoid patterning. The results dispute the role of retinoic acid (RA) in the specification and maintenance of UE, suggesting it to be inconsequential and unnecessary.

RESULTS

Nephrons and collecting duct structures arise through cell-specific differentiation and cross-inductive cues from posterior and anterior IM cell populations. To investigate, direct, and optimize these renal differentiation outcomes, we seeded the MBA with day 6 IM progenitors at 100,000 cells/cm^2, produced from HES3 cells by treatment with 8 μM Wnt agonist CHIR99201 for 2 days, followed by recombinant FGF9 (200 ng/ml) for 4 days (fig. S2A), as used by Takasato *et al.* (*1*). At 16 hours, these IM progenitors were assessed for paired box gene 2 (PAX2) and epithelial cadherin (ECAD) expression, confirming that all cells uniformly expressed PAX2 and no longer expressed epithelial cadherin (ECAD) (fig. S2, B and C). We observed that this IM cell population aggregates to form very similar colony-like structures in all wells over this time (fig. S2B). Image cytometry confirmed a uniform cell number distribution across all 270 wells with an average cell density across the MBA of $97 \times 10^3 \pm 2 \times 10^3$ cells/cm^2 corresponding to a 97% survival rate (fig. S2D). We next carried out a factorial screen for FGF9, BMP7, and RA. These molecules were chosen on the basis of outcomes of previous studies (*1*, *2*), suggesting a requirement for FGF9 in subsequent induction of kidney cell types from PAX2$^+$ECAD$^-$ IM, a poorly understood variable requirement for BMP7, while RA was thought to contribute to patterning of UE and nephrons (*3*). Furthermore, while the contributions of individual factors have been investigated, the potential interplay and relative impacts of these factors in combination are unknown.

We used the nested resistive network of the MBA to split and recombine input media containing these three factors at three concentrations (0, 50, and 100% of maximum working concentrations of 200 and 50 ng/ml and 0.1 μM, respectively), surveying 27 factorial factor combinations, for an additional 3 [referred to as day 9 MBAs (fig. S3A)] or 6 days [referred to as day 12 MBAs (Fig. 2A)]. These experiments were performed at a total media exchange rate of 480 μl/day, approximating that used in the static culture by Takasato *et al.* (*1*). Cells were fixed, counted, and phenotyped by in situ antibody labeling for GATA3, WT1, and ECAD (Figs. 1 and 2, C to E, and fig. S3, C to E). Image cytometry- and intensity-based gating was performed (as outlined in fig. S4) for each MBA replicate. The results from this classification, for the first rows of the day 9 and day 12 MBAs, can be seen in Fig. 3. At both time points, we readily identified several distinct cell types, including UE [WT1$^-$(Wilms tumor 1$^-$)GATA3$^+$(GATA Binding Protein 3$^+$)ECAD$^+$], MM (WT1$^+$ GATA3$^-$ECAD$^-$), early proximal nephrons (EPNs; WT1$^+$ GATA3$^-$ECAD$^+$), and early distal nephrons (EDNs; WT1$^-$GATA3$^-$ECAD$^+$). We also observed a

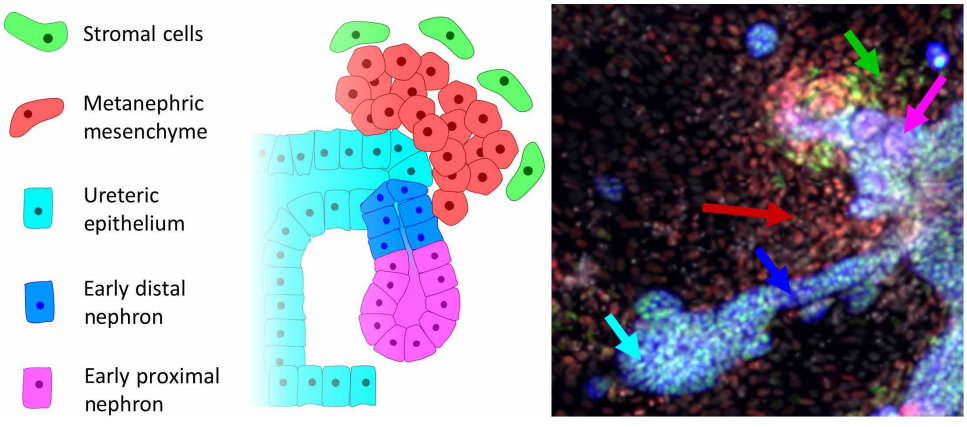

Fig. 1. A schematic of the early developing nephron and some key cell types: Schematic of nephron development. A small budding region begins to form on the UE (blue-green). MM (red) begins to condense into clusters around the budding UE structures. These clusters of MM begin forming comma-like structures and begin to show distal (EDN, blue) and proximal polarization (EPN, magenta). This structure migrates and merges with the tubular structure of the collecting duct. Stromal cells (SM, green) also begin to appear as a step toward vascularization.

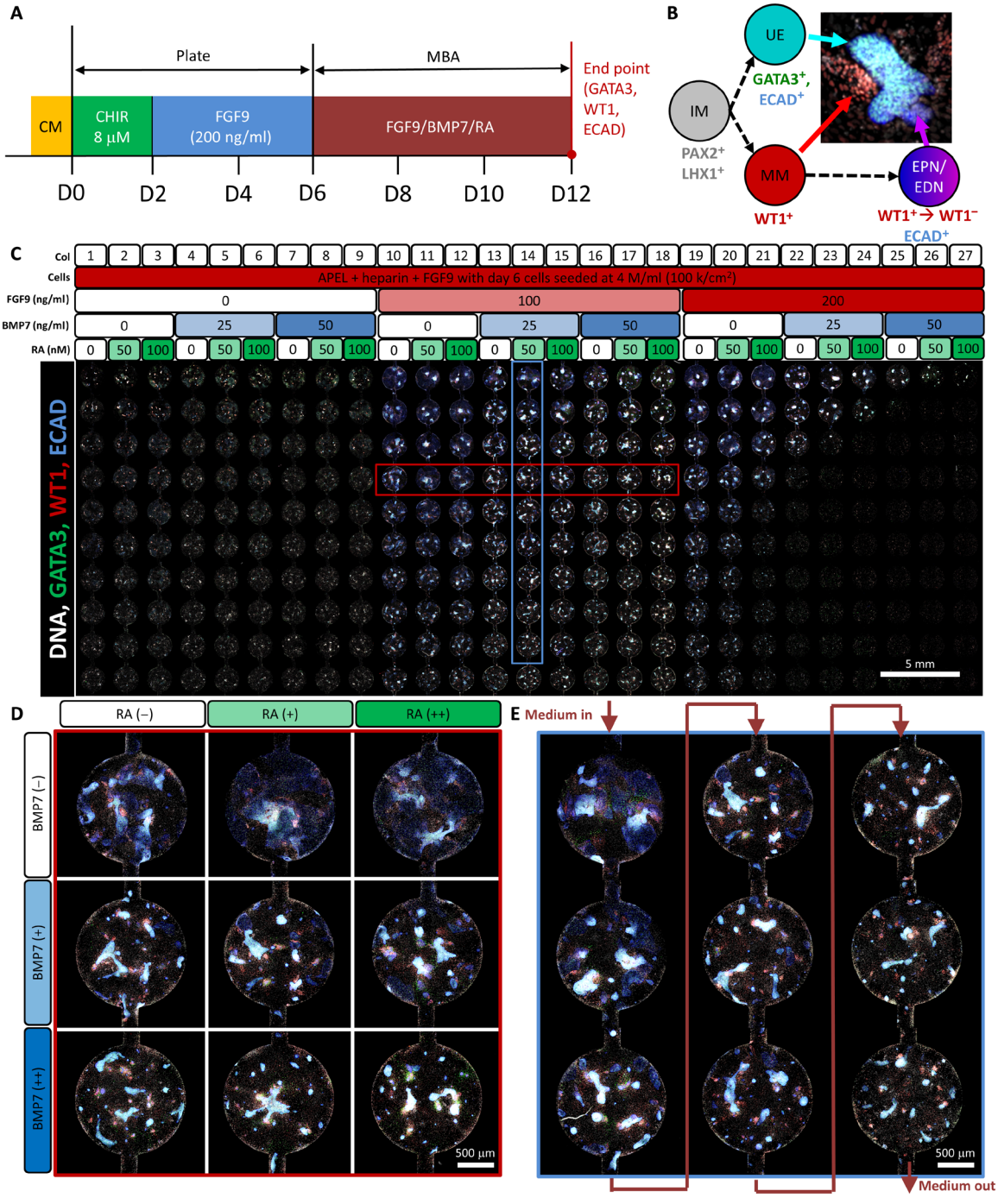

Fig. 2. Day 12 end point MBA stained for GATA3, WT1, and ECAD with the factorial input combination of FGF9, BMP7, and RA. (**A**) The experimental time course setup for the day 12 bioreactors. Here, cells were cultured in well plates for the first 6 days and in the MBA system for the following 6 days and stained for DNA (white), GATA3 (green), WT1 (red), and ECAD (blue). (**B**) A representation of two of the kidney cell subtypes being investigated: the MM ($WT1^+$) and the UE ($GATA3^+$ and $ECAD^+$) and their immunofluorescent representation. (**C**) The input of the MBA and subsequent immunofluorescence of each well. Even at a mesoscale view, it is clear that FGF9 is critical in the differentiation of IM cells toward kidney lineages. Furthermore, several cellular assemblies can be seen, which change in organization depending on the position within the MBA. (**D**) A zoomed-in view of nine wells along the fourth row of wells representing the intermediate concentration of FGF9 [red box shown in (C)]. Here, the effect of BMP7 and RA can be seen, which causes the condensation of the UE in tightly packed structures. (**E**). A zoomed-in view of nine sequential wells representing the intermediate concentration of FGF9, BMP7, and RA [blue box shown in (C)]. Here, similar changes in structures condensation of structures can be viewed as paracrine and autocrine factor accumulation occurs.

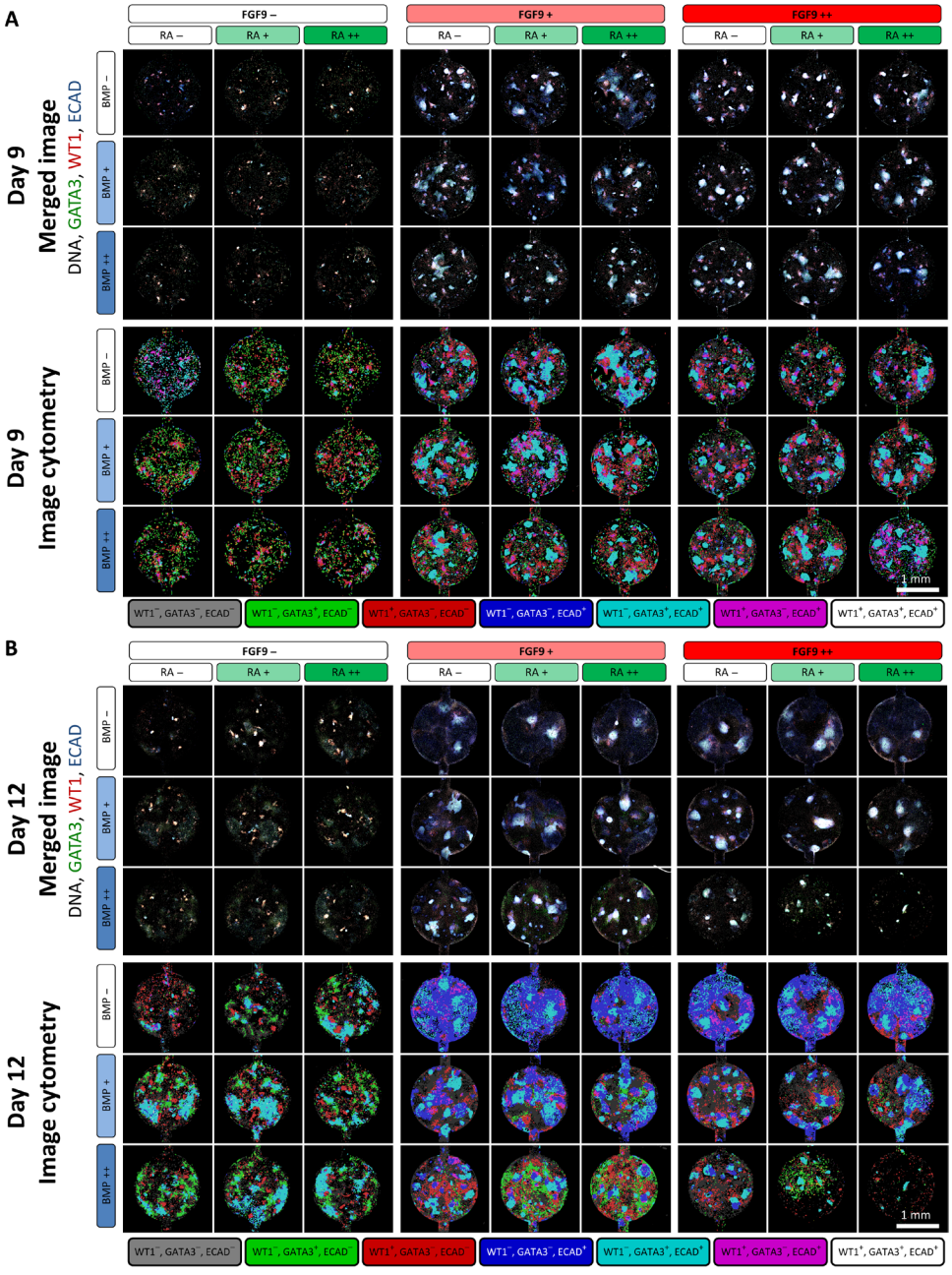

Fig. 3. Image cytometry comparison for the first row of the day 9 and day 12 bioreactors. (**A**) The immunofluorescent imaging of the first row of a day 9 MBA array with the variation of FGF9, BMP7, and RA as indicated and the corresponding image cytometry. Wells are stained with GATA3 (green), WT1 (red), and ECAD (blue). Here, the UE ($GATA3^+ECAD^+$), MM ($WT1^+$), EPNs ($WT1^+ECAD^+$), EDNs ($ECAD^+$), and mesangial cells ($GATA3^+$) can be identified, and small perturbations in the relative amounts of each phenotype can be seen. (**B**) The immunofluorescent imaging of the first row of a day 12 MBA array with the variation of FGF9, BMP7, and RA as indicated and the corresponding image cytometry with immunostaining as above.

population of $WT1^-GATA3^+ECAD^-$ cells representing stromal progenitor populations (*31*) and refer to them as presumptive stromal/mesangial cells (SM, $WT1^-GATA3^+ECAD^-$). Consistent trends were typically conserved between replicate MBAs and between day 9 and day 12 MBAs, except that 12-day culture in the MBA led to a significantly more complex and mature structure. To reveal the relative impacts and relationship of each parameter, we performed multivariate regression analysis for the total cell number and quantities of each of the kidney cell types.

Our multivariate regression analysis (Fig. 4 and fig. S5) shows that FGF9 is vital for cell proliferation and maintenance of all cell types. FGF9 is also crucial for generation of MM, EPN, EDN, and UE. All populations, except SM, were typically reduced in downstream wells in each column in response to (currently unknown) secreted paracrine factors. In the case of SM, its numbers increased at the day 9 and day 12 time points in response to secreted paracrine factors. The cell number reduced in downstream wells in response to paracrine signaling in the presence of FGF9. Because of the presence

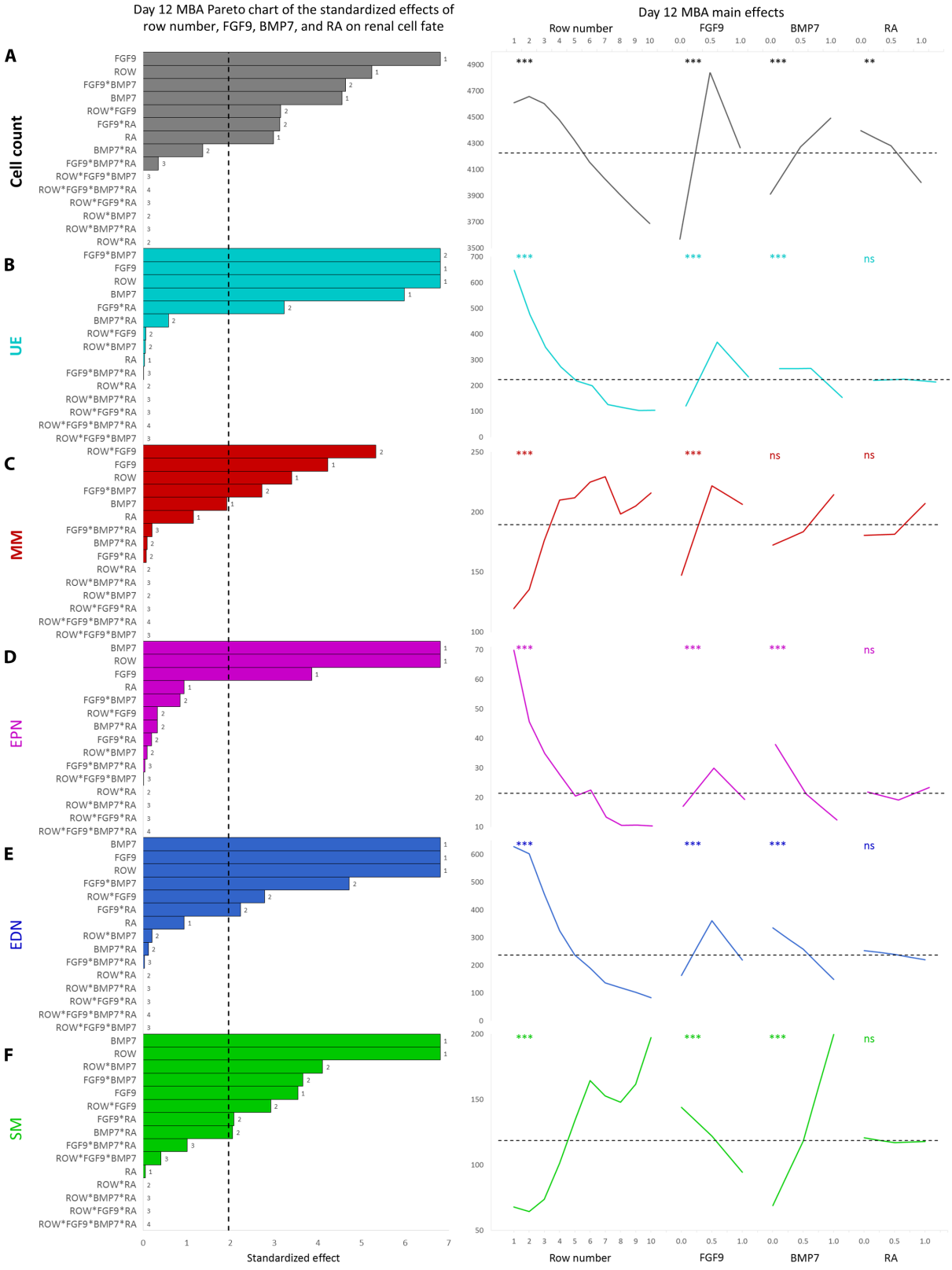

Fig. 4. Pareto chart of the standard effects and main effects plots from a full factorial design of experiment multivariate analysis day 12 MBAs. Pareto charts of all factors (row number, FGF9, BMP7, and RA) and their combinations and main effects of each input factor for the day 12 MBAs ($n = 4$). Phenotypical cell assessment included the cell count (**A**), UE (**B**), MM (**C**), EPN (**D**), EDN (**E**), and SM (**F**). The dashed line on each Pareto chart represents ($P = 0.05$), whereas the dashed line on the main effect plots represents the global mean of that parameter. *$P < 0.5$, **$P < 0.01$, and ***$P < 0.001$. ns, not significant.

of heparin in all of our experiments, it is unlikely that this is due to depletion of the FGF9 in lower rows, a phenomenon we previously confirmed that could be obviated with heparin sulfate fractions (extracted from heparin) with FGF2 (*26*). BMP7, on the other hand, increases the total cell number and proportion of SM and MM cells while significantly reducing EPN and EDN in day 9 MBAs (fig. S5). These trends were also reflected in the day 12 MBAs; however, the increase in MM was not significant (Fig. 4). Substantial variations in the morphology of structures within each well were observed, clearly a function of varying levels of BMP7 in the presence of FGF9 (Fig. 2D) and in response to paracrine signaling (Fig. 2E). Contrary to previous reports (*32*–*34*), across the 27 imposed factor combinations, we found that RA did not appear to play a role in early kidney differentiation. We considered that this failure of RA to affect kidney differentiation outcomes might depend on the short 2-day exposure to WNT activation, since under static culture conditions (*3*), increasing the duration of the initial CHIR99021 patterning mimicked posteriorization of the IM, resulting in a significant reduction in UE and an increase in $WT1^+HOXD11^+$ MM, an outcome that could be overcome via the addition of RA (*3*).

To investigate whether extended WNT activation would reveal a role for RA in renal differentiation when starting with posteriorized IM, we next extended CHIR treatment of HES3 cultures to 3 or 4 days before seeding in the MBA and thereafter continued culture for 5 days with FGF9 (200 ng/ml). These MBAs are referred to as day 3 to 8 and day 4 to 9 (Fig. 5A and fig. S6A, respectively). In addition to probing the impacts of extended exposure, we factorially assessed the impacts of RA, the pan-RAR (retinoic acid receptor) antagonist AGN194310 (hereafter AGN), as well as CHIR (Fig. 5B and fig. S6B). Prolonged stimulation with CHIR was included in this factorial screen since continued canonical Wnt activation has been previously proposed (*35*–*37*) to promote differentiation into of nephron progenitors.

On the basis of the size of the multicellular aggregates and the relative proportions of UE versus nephron structures [proximal nephron (PN) and distal nephron (DN)] across the MBA, it was clear that longer CHIR induction conditions, overall, resulted in a relative increase in mesenchymal elements and their derivatives at their end points (Fig. 5, C to E, and fig. S6, C to E), as compared to day 9 and day 12 MBAs (fig. S3C and Fig. 2C). Approximately 40% of the cells represented early nephrons in both day 3 to 8 and day 4 to 9 MBAs. Image cytometry of both day 3 to 8 and day 4 to 9 bioreactors showed a bias toward $WT1^+$ MM cells rather than $GATA3^+$ UE cells, consistent with the anticipated posterior IM shift (fig. S7).

Morphologically, these cells formed clusters of $WT1^+$ cells when seeded, which showed consistent reductions in size in response to paracrine signals from upstream wells in both day 3 to 8 and day 4 to 9 cells. However, day 3 to 8 and day 4 to 9 MBAs responded differently to prolonged WNT agonization (length of CHIR exposure). Overall, a negative correlation between prolonged WNT agonization and cell number exists, while other factors (AGN, RA, and paracrine signaling) have little influence on cell number (Fig. 6 and fig. S8). However, in day 4 to 9 MBAs, CHIR positively increased both UE and EDN populations while decreasing both MM and EPN populations (Fig. 6). This highlights the role of canonical Wnt signaling in biasing cells from proximal cell phenotypes (MM and EPN) toward distal cells phenotypes (UE and EDN), as has previously been proposed in mouse (*38*). In contrast, day 3 to 8 MBAs saw an increase in MM and no effect on UE while decreasing both EPN and EDN populations (fig. S8).

Paracrine signaling also differed between day 3 to 8 and day 4 to 9 MBAs. Cell number decreased in downstream wells in the day 3 to 8 MBAs, while it remained relatively constant in the day 4 to 9 MBAs (fig. S8). Day 4 to 9 MBAs showed increases in MM, UE, and EDN, while EPN remained relatively constant (Fig. 6). With day 3 to 9 MBAs, MM increased with additional paracrine signaling, while EPN and EDN decreased (fig. S8). Overall, UE decreased with paracrine signaling after small increases in the first few wells. The addition of AGN or RA had little effect on the presence of any phenotype (UE, MM, EPN, EDN, and SM) or cell number (Fig. 6 and fig. S8). Changes in the population of SM were negligible, as the population of these cells remained a small fraction (<0.1%) in all conditions in both day 3 to 8 and day 4 to 9 MBAs (Fig. 6 and fig. S8).

DISCUSSION

The capacity to accurately direct the differentiation of hPSCs to kidney tissue and individual kidney cell types represents a major opportunity for regenerative medicine and drug discovery. However, complex (often paracrine-mediated) differentiation events that direct renal cell type specification are difficult to replicate in standard static culture conditions. Here, we have taken advantage of our MBA platform that permits investigation of the impacts of these paracrine signaling events and that allows unbiased quantitative analysis of the relative impacts of factorial combinations of small molecules and growth factors on renal cell fate decisions.

Our novel approach, consisting of systematic analysis of more than 1000 unique biochemical input conditions from the four different MBA-based experiments, permitted rapid assessment of the relative effect of these unique input conditions on the expression of markers of kidney cell lineages, including ECAD, WT1, and GATA3, that, in combination, can identify UE, MM, EPN, EDN, and SM. We have summarized all of these sets of data as normalized and averaged heat maps in fig. S9 for observing MBA-wide phenotypical patterning. We also investigated the distribution of cellular aggregates within the MBAs; however, this has not demonstrated any distinct trends from the average number of cells per well (fig. S9). Our data reveal a clear role for Wnt signaling in the maintenance of the UE and the existence of several paracrine signaling events that have remained underappreciated in static culture. We note that this can only be attributed to biochemical cues, as we have verified constant flow rates columnwise and uniform cell seeding across the MBA. We have also performed experiments in which factor inputs are physically swapped, which shows trends owning to the inputted molecules effect and not the physical location in the MBA.

The design of the MBA is such that row 1 of each MBA column contains cells that only see the incoming factor combination and are most like conventional static plate-based conditions. When we examined row 1 of the day 9 and day 12 MBAs, we indeed observed a close coincidence between MBA outcomes and those previously observed in static culture (*1*), such as the requirement for FGF9, a positive effect of low and intermediate BMP7 concentrations for the generation of raised and cell-dense UE structures but a reduction in UE at high BMP7 levels. We further noted an increase of both SM and MM phenotypes in the presence of BMP7 and RA together, particularly in the day 12 MBAs with the highest BMP7 dose. However, all subsequent serially connected rows below are exposed to progressive accumulation of paracrine (secreted) factors plus the initial factors or modified versions thereof, including possible

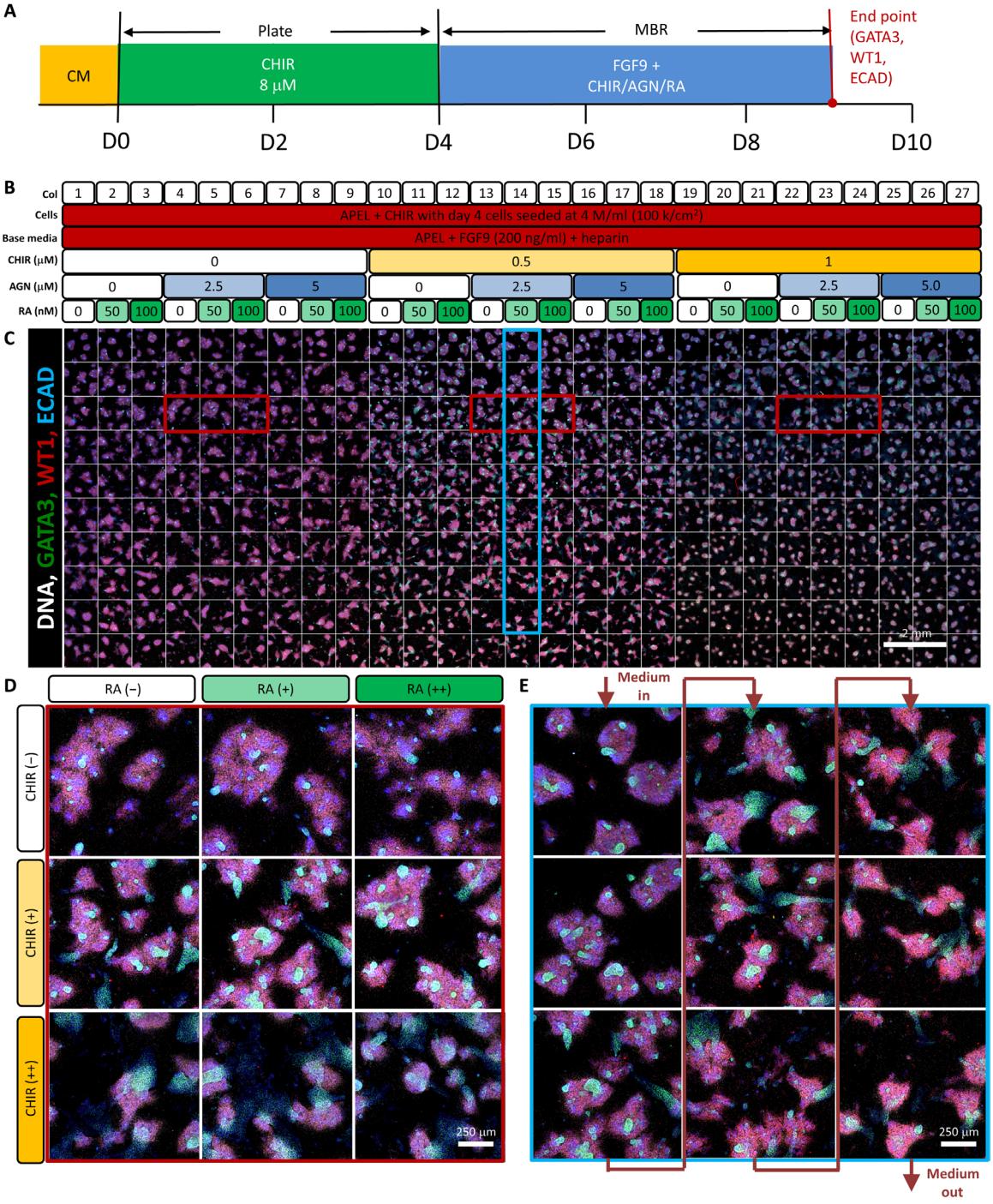

Fig. 5. Analysis of the effect of continued Wnt signaling and RA activity after variation in the initial duration of canonical Wnt patterning (4 days of initial CHIR, day 4 to 9 MBAs). (**A**) Experimental plan for 4-day CHIR induction with 5-day factorial analysis (day 4 to 9 MBAs). FGF9 was present across the entire 5-day period during the factorial perfusion. (**B**) The working concentrations of CHIR, AGN, and RA used for both MBA experiments (day 3 to 8 and day 4 to 9). (**C**) The full scan of each well of day 4 to 9 MBAs stained for GATA3 (green), WT1 (red), and ECAD (blue). (**D**) Representative wells from row 3 representing the effect of CHIR and RA with constant AGN. These wells are highlighted about in red on the overall scan. (**E**) Representative wells from column 14 representing the induced paracrine signaling. These wells are highlighted in blue on the overall scan.

depletion or inactivation of FGF9, BMP7, or RA synergistically. The experimental context explored in the MBA thus represents unique conditions unavailable to static plate cultures and thus previously unexplored in vitro. Given the substantial number of conditions explored in each MBA, we will first discuss the major effects of each factor and its interaction with other factors, based on the main effect of a given factor, and thereafter proceed to discuss paracrine impacts within a given column.

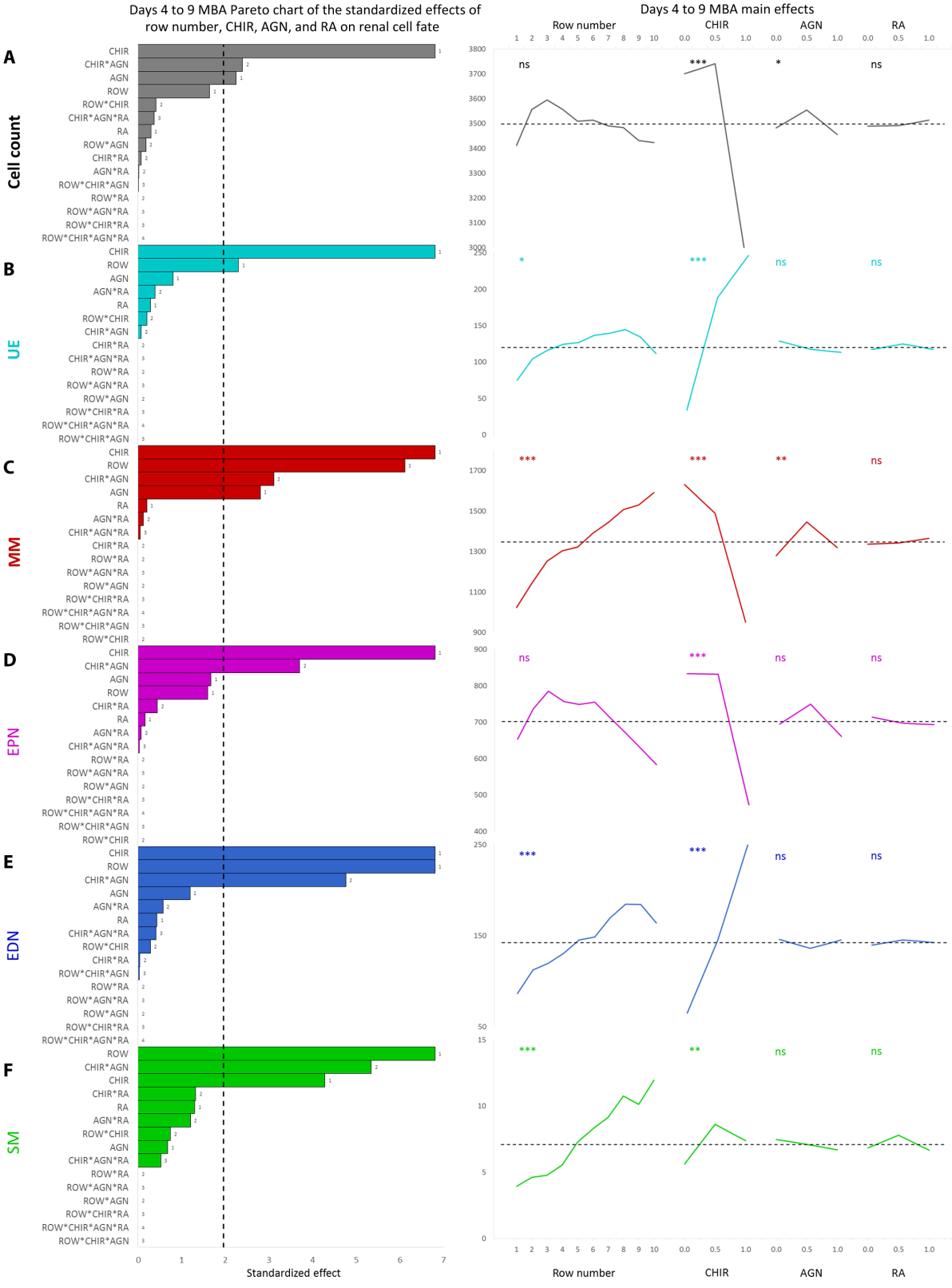

Fig. 6. Main effects plots from a full factorial design of experiments multivariate analysis for day 3 to 8 and day 4 to 9 MBAs. Pareto charts of all factors (row number, FGF9, BMP7, and RA) and their combinations and main effects of each input factor for the day 4 to 9 MBAs ($n = 4$). Phenotypical cell assessment included the cell count (**A**), UE (**B**), MM (**C**), EPN (**D**), EDN (**E**), and SM (**F**). The dashed line on each Pareto chart represents ($P = 0.05$), whereas the dashed line on the main effect plots represents the global mean of that parameter. *$P < 0.5$, **$P < 0.01$, and ***$P < 0.001$.

In both day 9 and day 12 MBAs, we show that that FGF9 plays a significant role in cell viability, renal fate, and cell number. We observe a global bias of cells toward UE (up to intermediate concentrations) and EDN cell subtypes when combined with an initial short Wnt activation (2 days) at day 9, whereas MM is inhibited at high FGF9 concentrations. This apparent role for FGF9 in the support of the UE over MM after initial short Wnt activation is not easily predicted from the literature. Moreover, FGF9 is expressed in the ureteric tip of the developing kidney and has been shown to support the MM (*3*). However, other FGFs are known to support the UE, and hence, FGF9 may be playing a generic role in stimulating FGF signaling in this instance. By day 12, however, we see that exogenous FGF9 is supporting MM at intermediate concentrations. These data suggest that initial FGF9 stimulation can induce UE specification, but once UE cells are present to sufficient levels, higher FGF9 concentrations become inhibitory.

EPN and MM populations were observable upon the inclusion of BMP7, which, in turn, generated significantly more complex cellular organization reminiscent of the early ureteric tree (Fig. 2). A role for BMP7, in both the maintenance of the MM and the formation of the nephrons, has been described in the developing mouse kidney (*39*) but appears to play an equally important role in human kidney patterning (*4*). We show that we can tune the relative cell subtype populations from a distal tubule population toward the proximal tubule by adding BMP7 in the presence of FGF9, after IM specification (2 days of CHIR, followed by 4 days of FGF9).

When the hPSCs were exposed to longer initial Wnt activation (day 3 to 8 and day 4 to 9 MBAs; Fig. 5 and fig. S6), cells in the presence of only FGF9 were biased toward proximal tubal cell subtypes (as opposed to more distal tubule-like with 2 days of CHIR), with only small clustered populations of UE present. When FGF9 and Wnt are activated simultaneously, these remaining UE clusters increased in size and organized into more complex structures, interacting with the remaining EPN and MM populations. This highlights that we can also tune the relative amounts of nephron versus UE by continued Wnt activation in the presence of FGF9. We would interpret this as the provision of a secreted support signal for the UE from the MM present in the well; however, the observed improvement of this scenario in the presence of prolonged CHIR (Figs. 5 and 6) suggests that this outcome may also result from a direct effect of the Wnt signaling on the UE. In contrast, RA signaling (either through addition of RA or blocking of the receptor with AGN) showed little effect on differentiation outcomes, independent of the previous exposure time to CHIR (or posterization of the IM).

Our data demonstrate that small step changes in exogenous (FGF9, BMP7, and CHIR) and endogenous (paracrine and autocrine) signaling can shift the ratio of ureteric, MM, and EPN and DN phenotypical cells from IM precursor cells. FGF9 signaling proved critical in maintaining all populations. The predominance of DN populations transitioning to PN populations is clearly seen in fig. S3C and Fig. 2 (C to E) with respect to BMP7 and paracrine/autocrine signaling. This effect is also quantified in Fig. 4 and fig. S5. In contrast, proximal to distal population shifts can be observed qualitatively in the day 4 to 9 MBAs, shown in Fig. 5 (C to E), as a direct consequence of both Wnt activation (CHIR addition) and paracrine/autocrine signaling. Quantitatively, both of these effects were demonstrated significantly in Fig. 6.

We can further discount the potential for input factor depletion because increasing concentrations of input factors do not result in increased conversion in a larger number of downstream rows to the same cellular outcomes in a given column. The two medium inputs that caused the most variation in the final cell phenotypes were FGF9 (day 9 and day 12 MBAs) and CHIR (day 3 to 8 and day 4 to 9 MBAs). We have summarized these effects for the day 12 and day 4 to 9 MBAs in fig. S10A. It is clear from the image cytometry data for these experiments that increased concentrations of FGF9 (day 12 data) or CHIR (day 4 to 9 data) do not result in increased penetrance of any of the cell types or structures, and moreover, these columns also beautifully show the impact of the media being conditioned by upstream wells as it flows into downstream wells (paracrine-mediated changes) in terms of changes to cell type, number, and organoid structure, which is explicitly different for each concentration of factor input.

Moreover, evidence of paracrine-mediated differences in cellular specification is demonstrated in column 1 of every MBA, which represents a 0,0,0 concentration condition of any of the input factors (fig. S10B). Differences between rows 1 and 10 in terms of the observed substantial loss or gain of cell types and changes in cell patterning can only be due to media conditioning/secreted factor accumulation in downstream rows, mediating changes in cell phenotype and tissue organization through paracrine actions. While the factors responsible for this paracrine action are not known, the outcomes observed are definitively paracrine mediated.

To exemplify that conditions highlighted within the MBA can be translated to standard plate-based culture formats, we have scaled up two of the conditions examined in the day 4 to 9 MBAs (columns 1 and 19) into 96-well plates. In the absence of detailed knowledge of the actual type and amounts of secreted factors and hence the extent of media conditioning, and the temporal impact of perfusion on the provision to and removal of these factors from cells in each well, it is unrealistic to expect that plate-based experiments will fully recapitulate the range of patterning outcomes achieved within a column of the MBA under perfusion. However, we would still expect similar trends. As seen in fig. S10C, we have confirmed that the same cell phenotypes in similar states of patterning as observed in some wells within the day 4 to 9 MBA columns are reproduced under the chosen validation conditions extracted from the MBA—the addition of CHIR decreases the total number of cells while biasing the population away from MM ($WT1^+ECAD^-$) and toward EDN ($ECAD^+$) and UE ($ECAD^+GATA3^+$). This is mirrored in the day 4 to 9 MBAs as distal nephrons increase from 3 (0.4 to 6% column range) to 14% (8 to 23% column range) with the addition of CHIR, while UE increases from 2.5 (0 to 5.6% column range) total to 13% percent (2 to 37% column range).

In this study, we selected three antibodies chosen for their capacity to multiplex to identify up to five distinct cell types. We must acknowledge that none of these proteins are specific to the kidney just as they are not completely specific to the putative kidney cell types that we have described an identity to here (*40*–*43*). However, what our data definitively confirm is that initial renal differentiation can be perturbed to bias the patterning and cellular complexity present in these renal differentiations, highlighting evidence for clear and complex paracrine signals that can shift cellular identity, cluster morphology, and spatial interactions between distinct cell types as well as the relative ratio of cell types within each condition. This approach does not demand or impede 3D formations from arising, thereby maintaining a capacity to facilitate cellular self-organization. It is clear that under these culture conditions, while the formation

of a homogeneous cellular identity is not occurring, in some cases (e.g., columns 10 to 12 and 19 to 21 in Fig. 2C and columns 1 to 9 in Fig. 5C), we are getting very close. Overall, our data support the concept that the processes observed in our MBAs replicate stepwise patterning like that in the embryo, with the requirement for multiple distinct cell types that signal between each other to arise across time.

We have demonstrated the utility of MBA-based factorial analyses of complex cellular mixes to tune the relative ratio of a given renal cell type. In the context of kidney differentiation, the tunability of this approach has provided clues on how to better pattern specific nephron segments for the eventual maturation of these cell types. A better appreciation of the identity of the paracrine signals arising within these MBAs may also help to uncover additional signals critical for renal cellular identity and/or maturation. We have shown this approach to be applicable to complex multistep differentiation cultures, requiring the simultaneous analysis of multicellular outcomes. Hence, this MBA-based factorial approach is likely to be valuable in the tuning of differentiation of other organoid-like induced pluripotent stem cell–derived tissues.

MATERIALS AND METHODS

Microfluidic device fabrication and preparation

The MBA was fabricated through standard soft lithography processes (*23*). The layout of this device can be seen in fig. S1 (A and B). Briefly, silicon wafers (Micro Materials and Research Consumables) were cleaned in an oxygen plasma in a custom reactive ion etcher (ANFF-Q) for 10 min at a pressure of 200 mtorr and 200 W. SU-8 2100 (MicroChem) was then spin-coated to a thickness of 100 μm and patterned as per the manufacturer's recommendations. All bake steps were ramped up and down to minimize stress and SU-8 thickness variation. This process formed the master for the soft lithographic process.

The master was then treated with chlorotrimethylsilane (CTMS, Sigma-Aldrich) each time before molding. This was accomplished by placing a few drops of CTMS on the master and allowing it to evaporate. Concurrently, polydimethylsiloxane (PDMS) base and curing agents (Sylgard 184, Dow Corning) were mixed and degassed. The PDMS mixture was then poured over the master, degassed to remove and residual bubbles, and then baked at 85°C for 20 min. A 100 mm by 75 mm glass slide (ProSciTech) was also spin-coated with a thin layer of PDMS and baked for 20 min at 85°C. Each layer of the device was cut to size, and holes were punched for inlets, outlets, and through holes with a 0.75-mm biopsy punch (ProSciTech).

All PDMS parts were cleaned with Scotch Magic tape (Scotch), before assembly. The device was then assembled by plasma-bonding the three pieces of the devices sequentially. That is, the bottom part of the device was bonded to the glass slide, followed by the bonding of the devices' top piece. All plasma bonding was performed in a plasma cleaner (Harrick) with an oxygen pressure of 400 to 500 mtorr for 30 s. All alignment was performed manually, and devices were allowed to bake at 65°C overnight to facilitate bonding. A final, filled device can be seen in fig. S1D. Devices were then autoclaved, dried, and stored before use.

Plugs and connective tubing were also custom-fabricated. Plugs consisted of a 22-g blunt needle (BRICO Medical Supplies) tubes separated from their top plastic bases and inserted into a 5-mm PDMS cylinder and autoclaved. All inlets and outlets were blocked with plugs while not in operation. Connective tubing consists of a 500-mm length of polyethylene tubing (PE50, BD Biosciences). Blunt needle tubes were inserted into one end of the tubing, while full blunt 22-g blunt needles were inserted to the other. Tubing was sterilized with 70% (v/v) ethanol and dried before use.

Human embryonic stem cell culture and initial differentiation

Human embryonic stem cells were maintained and expanded using conventional techniques as previously reported. A HES3-Mixl1 reporter line was cultured using standard techniques. Briefly, cells were expanded and maintained on irradiated mouse embryonic feeder cells (MEFs) in KSR (knockout serum replacement) media supplemented with basic FGF at 10 ng/ml. Cells were passaged enzymatically using TrypLE (Thermo Fisher Scientific, USA) for 3 min, followed by being rinsed in Dulbecco's minimum essential medium/F12. Before differentiation, cells were adapted to Matrigel-coated (Corning Life Sciences, USA) culturing techniques with MEF-conditioned KSR for one passage. Subsequently, cells were seed on Matrigel-coated six-well plates at a density of 12,000 cells/cm^2 in conditioned KSR. The following day, KSR media was replaced with APEL (albumin polyvinylalcohol essential lipids) media with 8 μM CHIR.

For "day 6" cells, CHIR treatment was carried out for 2 days. After 2 days, the media was aspirated and replaced with APEL with FGF9 (200 ng/ml) and heparin (50 μg/ml). Media was replaced after 2 days, and on the sixth day, cells were dissociated with TripLE, rinsed in media and resuspended as described above. These cells were seeded immediately in bioreactors as described below.

For "day 3/4" cells, CHIR treatment was carried out for 4 days in total, with fresh media replaced after 3 days. These cells were then dissociated with TripLE and rinsed and resuspended in APEL with 8 μM in each bioreactor as described below.

MBA differentiation

Immediately before use, MBA devices were submerged in phosphate-buffered saline (PBS, Lonza) with 1% antibiotic-antimycotic (AA) and placed in a vacuum desiccator for 20 min. The device was then removed from vacuum and allowed to fill for an hour. Once filled, the cell culture areas were coated with Matrigel for 20 to 40 min at 37°C. After coating, bioreactors were then resubmerged in PBS, and then 1 ml of either day 6 or day 4 cells were injected. The bioreactor was then plugged, and cells were allowed to attach for 16 hours.

Once the cells were adhered, the device was once again submerged in PBS, and the perfusion system was set up. Each experiment involved six inlets where each media stream was connected to a different syringe on a single multisyringe syringe pump (New Era). The initial perfusion was carried out at a total flow rate of 300 μl/hour for the first 300 μl to ensure a roughly equal starting exposure time to the inputted factors in their corresponding ports as specified by fig. S1 (A and C). The subsequent total flow rate used was 20 μl/hour, which corresponds to a media exchange rate equivalent to the changing of media once every 3 days in conventional culturing techniques.

For day 6 cells, the base media used was APEL with 1% AA. For these experiments, inlets A0, B0, and C0 were perfused with base media, while A1, B1, and C1 were perfused with base media supplemented with FGF9 (600 ng/ml), BMP7 (150 ng/ml), or 0.3 μM RA, respectively, as shown in Fig. 2B. For day 3/4, the base media used APEL with 1% AA and FGF9 (200 ng/ml). Once again, A0, B0, and C0 were perfused with day 4 base media, while A1, B1, and C1 were perfused

with base media supplemented with 3 μM CHIR and 15 μM and 0.3 μM RA, respectively, as shown in Fig. 5B.

Factor concentrations inputted into the bioreactor were diluted by a factor of 3 owing to the flow splitting and mixing within the device. Cells were perfused for between 3 and 6 days for day 9 and day 12 MBAs, respectively. Both day 3 to 8 and day 4 to 9 MBAs were perfused for a total of 5 days.

Immunofluorescence sample preparation

Once complete, the MBAs were prepared for immunofluorescence imaging. The volume of the MBA was exchanged within the device by slowly manually injecting the solution with a 1-ml syringe with a 22-gauge blunt needle through the cell seeding inlet to the cell seeding outlet. Cells were fixed in a two-stage process and carried out under chilled PBS. Initial fixation was carried out using 2% (weight) paraformaldehyde in PBS for 10 min. After three brief rinses with PBS, cells were then exposed to absolute ethanol for 15 min, followed by three more brief rinses with PBS.

Blocking buffer was prepared with 10% donkey serum (Sigma-Aldrich) and 0.3% Triton X-100 (Sigma-Aldrich) in PBS. Rinse buffer consisted of 1% donkey serum and 0.05% Tween 20 (Sigma-Aldrich) in PBS. Devices were blocked with blocking buffer for 1 hour at room temperature, followed by a rinse with the rinse buffer. Primary antibodies of GATA3 (R&D Systems), WT1 (Santa Cruz Biotechnology), ECAD (BD Biosciences), and/or PAX2 (Life Technologies) were all diluted at 1:200 in rinse buffer and allowed to adsorb overnight at 4°C. The devices were then rinsed three times with rinse buffer. Donkey (H+L) secondary antibodies of AF488 anti-goat, AF568 anti-rabbit, and AF647 anti-mouse (Life Technologies) at a dilution of 1:500 with Hoechst 33342 (Life Technologies) were diluted 1:1000 in rinse buffer and allowed to adsorb for 1.5 hours at room temperature. Devices were lastly rinsed three times with rinse buffer, followed by a single time with PBS.

Imaging

Devices were removed from the PBS bath and dried before being placed on a custom 3D-printed holder. This allowed the device to be placed in any image system compatible with standard tissue culture plates. All imaging took place on an LSM 710 (Carl Zeiss) confocal microscope. Each well was imaged sequentially with each fluorophore imaged separately. Nine uniformly distributed points throughout the bioreactor were taken to generate a focus map. Interpolation was then applied to get the *X*, *Y*, and *Z* positions of each of the 270 wells. For the day 3 to 8 and day 4 to 9 MBAs, *Z* stacks were used. The *Z* stacks focus was ensured to be at the bottom of each well, and subsequent images in the stacks were programmed to increment up from the bottom at a 10-μm increment.

Image cytometry and cell phenotyping

Image quantification was performed in CellProfiler, using custom-developed pipelines and MATLAB. Briefly, for each bioreactor, final image thresholds were manually set to reflect similar staining trends. These settings were conserved for each well of the bioreactor. For each well, nuclei were identified. The cell body was then approximated by use of a watershed around the cell nuclei to score non-nuclear staining. Each nucleus was then used to score its mean intensity of WT1 or GATA3, while its cell boundary was used to score its ECAD values. These values were then normalized by the mean intensity of the nuclear staining. Next, each cell was classified on the basis of manually set gating for each of the three markers used and were applied across each bioreactor. CellProfiler analyst density plots were generated to assist with thresholding. These values were set using several test images from random wells and bioreactor-wide histogram information. Cell classification images were then generated by combining the three binary maps generated by CellProfiler into a single image in MATLAB with $GATA3^+$, $WT1^+$, and $ECAD^+$, represented by the colors green, red, and blue, respectively, as shown in Fig. 5 and fig. S7. This entire process is outlined in fig. S4.

This allowed each well to be scored on the basis of percentage of positive and double-positive cells. Larger aggregates were also scored in a similar fashion, based on a larger size along with an image blur step. This was done for the WT1-positive clusters and the GATA3 clusters independently. This allowed for larger structures to be identified and investigated for cell number and size. All identification steps were validated and checked by the output of the cell or structure outline overlaid on the original image.

Factorial analysis and main effects plots

Phenotypical cell percentages and total cell numbers for each well of each bioreactor in each set were collated into large matrices organized for input into Minitab. A general factorial analysis was constructed with four factors: input A (FGF9 or CHIR, 3 values), input B (BMP7 or AGN, 3 values), input C (RA, 3 values), and input D (row number/paracrine factors, 10 values). For each dataset, there were between two and four replicates. Data were randomized and transformed with a Box-Cox transformation (λ set to optimal), and subsequent normality was confirmed. Standardized Pareto charts were generated, and main effects plots were generated and adapted to fit on a single plot, while interaction plots failed to show clear or significant trends. Plots generated were shown in Figs. 4 and 6 and figs. S5 and S8.

SUPPLEMENTARY MATERIALS

Supplementary material for this article is available at http://advances.sciencemag.org/cgi/content/full/6/2/eaaw2746/DC1

Fig. S1. MBA design, layout, and operation.
Fig. S2. Initial bioreactor seeding with $PAX2^+$ cell population.
Fig. S3. The day 9 end point MBA.
Fig. S4. The process flow for the MBA image cytometry.
Fig. S5. Pareto chart of the standard effects and the main effects plots from a full factorial design of experiments multivariate analysis day 9 MBAs.
Fig. S6. Analysis of the effect of continued Wnt signaling and RA activity after variation in the initial duration of canonical Wnt patterning (3 days initial CHIR).
Fig. S7. Image cytometry comparison for the first row of the day 3 to 8 and day 4 to 9 MBAs.
Fig. S8. Pareto chart of the standard effects and the main effects plots from a full factorial design of experiments multivariate analysis day 3 to 8 MBAs.
Fig. S9. Heat maps of cell distributions with all MBA sets (day 9, day 12, days 3 to 8, and days 4 to 9).
Fig. S10. Investigating the paracrine and autocrine effect in the MBAs.

View/request a protocol for this paper from *Bio-protocol*.

REFERENCES AND NOTES

1. M. Takasato, P. X. Er, M. Becroft, J. M. Vanslambrouck, E. G. Stanley, A. G. Elefanty, M. H. Little, Directing human embryonic stem cell differentiation towards a renal lineage generates a self-organizing kidney. *Nat. Cell Biol.* **16**, 118–126 (2014).
2. M. Takasato, M. H. Little, The origin of the mammalian kidney: Implications for recreating the kidney in vitro. *Development* **142**, 1937–1947 (2015).
3. M. Takasato, P. X. Er, H. S. Chiu, B. Maier, G. J. Baillie, C. Ferguson, R. G. Parton, E. J. Wolvetang, M. S. Roost, S. M. Chuva de Sousa Lopes, M. H. Little, Kidney organoids from human iPS cells contain multiple lineages and model human nephrogenesis. *Nature* **526**, 564–568 (2015).
4. Y. Xia, E. Nivet, I. Sancho-Martinez, T. Gallegos, K. Suzuki, D. Okamura, M.-Z. Wu, I. Dubova, C. R. Esteban, N. Montserrat, J. M. Campistol, J. C. Izpisua Belmonte, Directed differentiation of human pluripotent cells to ureteric bud kidney progenitor-like cells. *Nat. Cell Biol.* **15**, 1507–1515 (2013).

5. A. Taguchi, Y. Kaku, T. Ohmori, S. Sharmin, M. Ogawa, H. Sasaki, R. Nishinakamura, Redefining the in vivo origin of metanephric nephron progenitors enables generation of complex kidney structures from pluripotent stem cells. *Cell Stem Cell* **14**, 53–67 (2014).
6. R. Morizane, A. Q. Lam, B. S. Freedman, S. Kishi, M. T. Valerius, J. V. Bonventre, Nephron organoids derived from human pluripotent stem cells model kidney development and injury. *Nat. Biotechnol.* **33**, 1193–1200 (2015).
7. B. S. Freedman, C. R. Brooks, A. Q. Lam, H. Fu, R. Morizane, V. Agrawal, A. F. Saad, M. K. Li, M. R. Hughes, R. V. Werff, D. T. Peters, J. Lu, A. Baccei, A. M. Siedlecki, M. T. Valerius, K. Musunuru, K. M. McNagny, T. I. Steinman, J. Zhou, P. H. Lerou, J. V. Bonventre, Modelling kidney disease with CRISPR-mutant kidney organoids derived from human pluripotent epiblast spheroids. *Nat. Commun.* **6**, 8715 (2015).
8. S. M. Czerniecki, N. M. Cruz, J. L. Harder, R. Menon, J. Annis, E. A. Otto, R. E. Gulieva, L. V. Islas, Y. K. Kim, L. M. Tran, T. J. Martins, J. W. Pippin, H. Fu, M. Kretzler, S. J. Shankland, J. Himmelfarb, R. T. Moon, N. Paragas, B. S. Freedman, High-throughput screening enhances kidney organoid differentiation from human pluripotent stem cells and enables automated multidimensional phenotyping. *Cell Stem Cell* **22**, 929–940.e4 (2018).
9. V. Sanchez-Freire, A. D. Ebert, T. Kalisky, S. R. Quake, J. C. Wu, Microfluidic single-cell real-time PCR for comparative analysis of gene expression patterns. *Nat. Protoc.* **7**, 829–838 (2012).
10. A. K. White, M. VanInsberghe, O. I. Petriv, M. Hamidi, D. Sikorski, M. A. Marra, J. Piret, S. Aparicio, C. L. Hansen, High-throughput microfluidic single-cell RT-qPCR. *Proc. Natl. Acad. Sci. U.S.A.* **108**, 13999–14004 (2011).
11. H. L. T. Lee, P. Boccazzi, R. J. Ram, A. J. Sinskey, Microbioreactor arrays with integrated mixers and fluid injectors for high-throughput experimentation with pH and dissolved oxygen control. *Lab Chip* **6**, 1229–1235 (2006).
12. Z. Zhang, N. Szita, P. Boccazzi, A. J. Sinskey, K. F. Jensen, A well-mixed, polymer-based microbioreactor with integrated optical measurements. *Biotechnol. Bioeng.* **93**, 286–296 (2006).
13. P. Harms, Y. Kostov, J. A. French, M. Soliman, M. Anjanappa, A. Ram, G. Rao, Design and performance of a 24-station high throughput microbioreactor. *Biotechnol. Bioeng.* **93**, 6–13 (2006).
14. E. Tumarkin, L. Tzadu, E. Csaszar, M. Seo, H. Zhang, A. Lee, R. Peerani, K. Purpura, P. W. Zandstra, E. Kumacheva, High-throughput combinatorial cell co-culture using microfluidics. *Integr. Biol.* **3**, 653–662 (2011).
15. A. M. Taylor, M. Blurton-Jones, S. W. Rhee, D. H. Cribbs, C. W. Cotman, N. L. Jeon, A microfluidic culture platform for CNS axonal injury, regeneration and transport. *Nat. Methods* **2**, 599–605 (2005).
16. D. M. Titmarsh, N. R. Glass, R. J. Mills, A. Hidalgo, E. J. Wolvetang, E. R. Porrello, J. E. Hudson, J. J. Cooper-White, Induction of human iPSC-derived cardiomyocyte proliferation revealed by combinatorial screening in high density microbioreactor arrays. *Sci. Rep.* **6**, 24637 (2016).
17. D. M. Titmarsh, H. Chen, E. J. Wolvetang, J. J. Cooper-White, Arrayed cellular environments for stem cells and regenerative medicine. *Biotechnol. J.* **8**, 167–179 (2013).
18. D. O. Freytes, G. Vunjak-Novakovic, in *Biophysical Regulation of Vascular Differentiation and Assembly* 203–225 (Springer, 2011).
19. Y. Wen, X. Zhang, S.-T. Yang, Microplate-reader compatible perfusion microbioreactor array for modular tissue culture and cytotoxicity assays. *Biotechnol. Prog.* **26**, 1135–1144 (2010).
20. M. M. Maharbiz, W. J. Holtz, R. T. Howe, J. D. Keasling, Microbioreactor arrays with parametric control for high-throughput experimentation. *Biotechnol. Bioeng.* **85**, 376–381 (2004).
21. R. Gómez-Sjöberg, A. A. Leyrat, D. M. Pirone, C. S. Chen, S. R. Quake, Versatile, fully automated, microfluidic cell culture system. *Anal. Chem.* **79**, 8557–8563 (2007).
22. L. Kim, M. D. Vahey, H.-Y. Lee, J. Voldman, Microfluidic arrays for logarithmically perfused embryonic stem cell culture. *Lab Chip* **6**, 394–406 (2006).
23. D. M. Titmarsh, J. E. Hudson, A. Hidalgo, A. G. Elefanty, E. G. Stanley, E. J. Wolvetang, J. J. Cooper-White, Microbioreactor arrays for full factorial screening of exogenous and paracrine factors in human embryonic stem cell differentiation. *PLOS ONE* **7**, e52405 (2012).
24. D. Titmarsh, J. Cooper-White, Microbioreactor array for full-factorial analysis of provision of multiple soluble factors in cellular microenvironments. *Biotechnol. Bioeng.* **104**, 1240–1244 (2009).
25. D. M. Titmarsh, D. A. Ovchinnikov, E. J. Wolvetang, J. J. Cooper-White, Full factorial screening of human embryonic stem cell maintenance with multiplexed microbioreactor arrays. *Biotechnol. J.* **8**, 822–834 (2013).
26. D. M. Titmarsh, C. L. L. Tan, N. R. Glass, V. Nurcombe, J. J. Cooper-White, S. M. Cool, Microfluidic screening reveals heparan sulfate enhances human mesenchymal stem cell growth by modulating fibroblast growth factor-2 transport. *Stem Cells Transl. Med.* **6**, 1178–1190 (2017).
27. J. E. Frith, D. M. Titmarsh, H. Padmanabhan, J. J. Cooper-White, Microbioreactor array screening of Wnt modulators and microenvironmental factors in osteogenic differentiation of mesenchymal progenitor cells. *PLOS ONE* **8**, e82931 (2013).
28. J. Trott, E. K. Tan, S. Ong, D. M. Titmarsh, S. L. I. J. Denil, M. Giam, C. K. Wong, J. Wang, M. Shboul, M. Eio, J. Cooper-White, S. M. Cool, G. Rancati, L. W. Stanton, B. Reversade, N. R. Dunn, Long-term culture of self-renewing pancreatic progenitors derived from human pluripotent stem cells. *Stem Cell Rep.* **8**, 1675–1688 (2017).
29. A. E. Carpenter, T. R. Jones, M. R. Lamprecht, C. Clarke, I. H. Kang, O. Friman, D. A. Guertin, J. H. Chang, R. A. Lindquist, J. Moffat, P. Golland, D. M. Sabatini, CellProfiler: Image analysis software for identifying and quantifying cell phenotypes. *Genome Biol.* **7**, R100 (2006).
30. L. Kamentsky, T. R. Jones, A. Fraser, M.-A. Bray, D. J. Logan, K. L. Madden, V. Ljosa, C. Rueden, K. W. Eliceiri, A. E. Carpenter, Improved structure, function and compatibility for CellProfiler: Modular high-throughput image analysis software. *Bioinformatics* **27**, 1179–1180 (2011).
31. A. N. Combes, B. Phipson, L. Zappia, K. T. Lawlor, P. X. Er, A. Oshlack, M. H. Little, High throughput single cell RNA-seq of developing mouse kidney and human kidney organoids reveals a roadmap for recreating the kidney. *bioRxiv*, 235499 (2017).
32. M. Takayama, K. Miyatake, E. Nishida, Identification and characterization of retinoic acid-responsive genes in mouse kidney development. *Genes Cells* **19**, 637–649 (2014).
33. V. K. Nagalakshmi, J. Yu, The ureteric bud epithelium: Morphogenesis and roles in metanephric kidney patterning. *Mol. Reprod. Dev.* **82**, 151–166 (2015).
34. T. Bohnenpoll, A.-C. Weiss, M. Labuhn, T. H. Lüdtke, M.-O. Trowe, A. Kispert, Retinoic acid signaling maintains epithelial and mesenchymal progenitors in the developing mouse ureter. *Sci. Rep.* **7**, 14803 (2017).
35. A. C. Brown, S. D. Muthukrishnan, L. Oxburgh, A synthetic niche for nephron progenitor cells. *Dev. Cell* **34**, 229–241 (2015).
36. S. Tanigawa, A. Taguchi, N. Sharma, A. O. Perantoni, R. Nishinakamura, Selective in vitro propagation of nephron progenitors derived from embryos and pluripotent stem cells. *Cell Rep.* **15**, 801–813 (2016).
37. Z. Li, T. Araoka, J. Wu, H.-K. Liao, M. Li, M. Lazo, B. Zhou, Y. Sui, M.-Z. Wu, I. Tamura, Y. Xia, E. Beyret, T. Matsusaka, I. Pastan, C. R. Esteban, I. Guillen, P. Guillen, J. M. Campistol, J. C. I. Belmonte, 3D culture supports long-term expansion of mouse and human nephrogenic progenitors. *Cell Stem Cell* **19**, 516–529 (2016).
38. N. O. Lindström, M. L. Lawrence, S. F. Burn, J. A. Johansson, E. R. M. Bakker, R. A. Ridgway, C.-H. Chang, M. J. Karolak, L. Oxburgh, D. J. Headon, O. J. Sansom, R. Smits, J. A. Davies, P. Hohenstein, Integrated β-catenin, BMP, PTEN, and Notch signalling patterns the nephron. *eLife* **4**, e04000 (2015).
39. T. Tsujimura, M. Idei, M. Yoshikawa, O. Takase, K. Hishikawa, Roles and regulation of bone morphogenetic protein-7 in kidney development and diseases. *World J. Stem Cells* **8**, 288–296 (2016).
40. C. W. van den Berg, L. Ritsma, M. C. Avramut, L. E. Wiersma, B. M. van den Berg, D. G. Leuning, E. Lievers, M. Koning, J. M. Vanslambrouck, A. J. Koster, S. E. Howden, M. Takasato, M. H. Little, T. J. Rabelink, Renal subcapsular transplantation of PSC-derived kidney organoids induces neo-vasculogenesis and significant glomerular and tubular maturation in vivo. *Stem Cell Rep.* **10**, 751–765 (2018).
41. P. P. Pandolfi, M. E. Roth, A. Karis, M. W. Leonard, E. Dzierzak, F. G. Grosveld, J. D. Engel, M. H. Lindenbaum, Targeted disruption of the GATA3 gene causes severe abnormalities in the nervous system and in fetal liver haematopoiesis. *Nat. Genet.* **11**, 40–44 (1995).
42. Y. Wu, P. Kanchanawong, R. Zaidel-Bar, Actin-delimited adhesion-independent clustering of E-cadherin forms the nanoscale building blocks of adherens junctions. *Dev. Cell* **32**, 139–154 (2015).
43. J. M. Vieira, S. Howard, C. Villa del Campo, S. Bollini, K. N. Dubé, M. Masters, D. N. Barnette, M. Rohling, X. Sun, L. E. Hankins, D. Gavriouchkina, R. Williams, D. Metzger, P. Chambon, T. Sauka-Spengler, B. Davies, P. R. Riley, BRG1-SWI/SNF-dependent regulation of the Wt1 transcriptional landscape mediates epicardial activity during heart development and disease. *Nat. Commun.* **8**, 16034 (2017).

Acknowledgments: This work was partly performed at the Australian National Fabrication Facility, a company established under the National Collaborative Research Infrastructure Strategy to provide nano- and microfabrication facilities for Australia's researchers. **Funding:** We acknowledge the Australian Research Council Special Research Initiatives Scheme (SR1101002, Stem Cells Australia, http://stemcellsaustralia.edu.au), Organovo Inc., and the National Health and Medical Research Council of Australia (APP1041277) for funding. **Author contributions:** Conceived and designed the experiments: N.R.G., D.M.T., A.H., M.T., E.J.W., M.H.L., and J.J.C.-W. Performed the experiments: N.R.G., M.T., and P.X.E. Provided reagents/materials/analysis tools: N.R.G.,

M.T., and P.X.E. Processed and analyzed the data: N.R.G. and D.M.T. Wrote the manuscript: N.R.G., M.H.L., and J.J.C.-W. Edited the manuscript: N.R.G., D.M.T., A.H., M.T., E.J.W., M.H.L., and J.J.C.-W. Provided financial support: E.J.W., M.H.L., and J.J.C.-W. **Competing interests:** The authors declare that D.M.T. and J.J.C-.W. are listed as inventors on an International Patent Application related to the work, number WO2013036997 (13 September 2012). D.M.T. and J.J.C.-.W. are founders, officers, employees (D.M.T.), and stockholders of Scaled Biolabs Inc. M.H.L. and M.T. are listed as inventors on two International Patent Applications related to the work, number WO2014197934A1 (13 June 2014) and WO2016094948A1 (15 December 2015). These patents are entitled "Renal progenitor cells" and "Differentiation of pluripotent stem cells to form renal organoids." The authors declare no other competing financial interests. **Data and materials availability:** All data needed to evaluate the conclusions in the paper are present in the paper and/or the Supplementary Materials. Additional data related to this paper may be requested from the authors.

Submitted 4 December 2018
Accepted 30 October 2019
Published 8 January 2020
10.1126/sciadv.aaw2746

Citation: N. R. Glass, M. Takasako, P. X. Er, D. M. Titmarsh, A. Hidalgo, E. J. Wolvetang, M. H. Little, J. J. Cooper-White, Multivariate patterning of human pluripotent cells under perfusion reveals critical roles of induced paracrine factors in kidney organoid development. *Sci. Adv.* **6**, eaaw2746 (2020).